

Zare-Behtash, H., Kontis, K., Gongora-Orozco, N., and Takayama, K. (2010) *Shock wave induced vortex loops emanating from nozzles with singular corners*. Experiments in Fluids, 49 (5). pp. 1005-1019. ISSN 0723-4864 (doi:10.1007/s00348-010-0839-7)

Copyright © 2010 Springer Verlag

A copy can be downloaded for personal non-commercial research or study, without prior permission or charge

Content must not be changed in any way or reproduced in any format or medium without the formal permission of the copyright holder(s)

When referring to this work, full bibliographic details must be given

<http://eprints.gla.ac.uk/84643/>

Deposited on: 07 January 2014

# Shock wave induced vortex loops emanating from nozzles with singular corners

H. Zare-Behtash

*Spirit Aerosystems (UK), Prestwick International Airport, Ayrshire, KA9 2RW, UK*

K. Kontis\* and N. Gongora-Orozco

*School of MACE, The University of Manchester, M60 1QD, UK*

K. Takayama

*Tohoku University, Shock Wave Research Centre, Sendai 980-8577, Japan*

## Abstract

The focus of the current study is to examine experimentally the diffracted shock wave pattern and the consequent vortex loop formation, propagation, and decay from nozzles having singular corners. Non-intrusive qualitative and quantitative techniques: schlieren, shadowgraphy, and particle image velocimetry (PIV) are employed to analyse the induced flow fields. Eye-shaped nozzles were used with the corner joints representing singularities. The length of the minor axes are  $a = 6$  and  $15$  mm, with the major axis  $b = 30$  mm for both cases. The experiments are performed for flow Reynolds numbers in the range  $0.8 \times 10^5$  and  $4.6 \times 10^5$ . Air is used in both driver and driven sections of the shock tube.

---

\*k.kontis@manchester.ac.uk

## I. INTRODUCTION

Shock waves can occur either naturally or artificially. Examples of naturally occurring shocks are those due to volcanic eruptions and lightning bolts, or at much larger scale those due to violent solar eruptions which trigger interplanetary shocks.<sup>1</sup> A well known example of man made shock waves is that created from detonations. Detonations are distinguished from shock waves by the presence of an intrinsic length scale associated with a reaction zone.<sup>2</sup> The study into the evolution of detonation waves that suddenly expand has been motivated not only by the need to suppress accidental detonations but also in the interest of the applicability of such flows to the concept of pulse detonation engines (PDEs).<sup>3,4</sup> Upon diffraction of the detonation wave, a vortex loop is formed immediately behind it. Naturally occurring vortex loops form during the eruption of volcanos and consist of steam, ashes, and hot gases. Once created, vortex loops are self-contained, auto motive and quite long-lived.<sup>5</sup>

No matter the initial conditions in which a vortex loop is generated, there are three stages in the propagation of a vortex loop: formation, development, and decay. Although numerous authors have reported both experimental and numerical studies on vortex loop characteristics covering the incompressible,<sup>6–12</sup> compressible,<sup>13,14</sup> and detonation regimes,<sup>15</sup> there is a scarcity of data on compressible vortex loops and jets generated from nozzles with singular corners. Compressibility alone has a great influence in the propagation of vortex loops. The work of Moore 1985<sup>16</sup> showed that the effect of compressibility is to reduce the translational velocity of the axisymmetric vortex loops. A property which will be examined in the present study for non-axisymmetric vortex loops.

The numerical simulations of Takayama et al. 1993<sup>17</sup> of compressible vortex loop propagation and interactions agreed well with the corresponding pattern of experimental shadowgraphs. However, the lack of quantitative data in their work precluded quantitative validation of their simulations. The lack of data regarding the velocity and vorticity fields associated with compressible vortical flows was also evident in the simulations of Minota et al. 1997<sup>18</sup> and Tokugawa et al. 1997.<sup>19</sup> A feature which almost all the numerical work mentioned have in common is the assumption of axisymmetry of the flow, therefore requiring computations of only half the numerical domain. When dealing with compressible circular vortex loops this assumption only suffices during the initial stages of propagation before the flow becomes three dimensional owing to the instabilities developed or when dealing with

interactions such as shock-vortex interactions.<sup>20</sup> Even the relatively more recent numerical work performed on vortex loops although have taken compressibility into account have been focused on the sound generated through shock-vortex<sup>21</sup> or vortex-wall<sup>22</sup> interactions and did not deal with the unsteady velocity and vorticity fields associated with the vortex loops alone.

In conclusion, there appears to be a lack of quantitative data relating the velocity and vorticity fields associated with non-axisymmetric compressible vortex loops. This void is both in the experimental area to validate the findings of numerical simulations, and also in the numerical simulation domain to provide a more detailed insight into the flow properties; since experimental techniques have certain limitations on resolution. In the following cold-flow study we examine the diffracted shock wave pattern and the resulting vortex loop emitted from shock tubes of various geometries. Qualitative (schlieren and shadowgraphy) and the quantitative particle image velocimetry (PIV) techniques have been utilised to study and most importantly quantify the characteristic behaviour associated with the shock waves and vortex loops generated from nozzles with singularities. The effect of compressibility on the propagation of the vortex loops is also examined.

## II. EXPERIMENTAL SETUP

### A. Shock Tube

Experiments were carried out using air as both the driver and driven gas with diaphragm pressure ratios  $P_4/P_1 = 4, 8$  and  $12$ . With  $P_4$  being the pressure within the driving compartment of the shock tube, and  $P_1$  the pressure inside the driven section.

An industrial film diaphragm divides the two sections of the shock tube. The thickness of the diaphragms was chosen to be  $23, 55$ , and  $75 \mu m$  for  $P_4/P_1 = 4, 8$  and  $12$ , respectively. The diaphragm thickness corresponding to each pressure ratio was the minimum thickness which would sustain the desired pressure without spontaneously rupturing. The bursting of the diaphragm was initiated manually with a plunger.

Two exotic nozzles resembling eyes as shown in Figure 1, were designed and manufactured at the Shock Waves Research Centre in Tohoku University. Figures 1(a) and 1(b) show photographs of the two nozzles both having major axis of  $b = 30$  mm and minor axis  $a = 6$

and 15 mm, respectively.

The length of the circular driven section (baseline) of the shock tube where the exotic nozzles were attached was 1310.5 mm, with an internal diameter  $d_i = 30$  mm and outer diameter  $d_o = 38$  mm. The nozzles follow a smooth transition from the circular baseline case over a length of 300 mm to the two different exit geometries shown in Figure 1. The critical length of the driver section for the baseline section of the shock tube was  $12.3d_i$ ,  $8.53d_i$ , and  $7.23d_i$  for  $P_4/P_1 = 4$ , 8, and 12, respectively. Using the critical driver length ensures that the rarefaction wave reflected off the driver's end wall does not reach the shock tube open end (where the nozzle is) for a specified period of time. This produces a pulsed upstream condition where the duration and magnitude of the pulse can be controlled up to the nozzles' inlet.<sup>23–25</sup>

### **B. Schlieren and Shadowgraph Photography**

High-speed schlieren and shadow photography<sup>26</sup> were employed to visualise the induced flow-field. Schlieren and shadowgraphy are two techniques that complement each other, hence, they are used in parallel in the current study. The schlieren and shadowgraphy setup was identical to that used by Kontis et al. 2008<sup>27</sup> and details of the setup can be found therein. Schlieren and shadowgraph images were acquired for instances where the major axis of the nozzles were horizontal and vertical to provide a more complete picture of the flow development.

### **C. Particle Image Velocimetry**

In contrast to techniques for the measurement of flow velocities employing probes such as pressure tubes or hot wires, the particle image velocimetry (PIV) technique being an optical technique works non-intrusively. PIV is based on the measurement of the velocity of tracer particles carried by the fluid.<sup>28</sup> For the current study a high frame rate PIV system capable of capturing 1500 frames per second at  $1024 \times 1024$  pixels resolution was utilised. A high repetition rate laser (10 mJ at 1 kHz, Nd:YAG) with a light and a range of light sheet optics was used for illumination of the tracer particles. A Photron APX RS high frame rate camera was used to capture the images of the tracer particles. A model 9306A *TSI* six-jet atomizer

was used to generate the seeder particles using olive oil.

An estimation of how strictly the seed particles follow the flow and how fast the seed particles respond to the flow changes can be made utilising the particle Stokes number,  $St$ , which is the ratio of the particle relaxation time  $\tau_p$  to the characteristic time of the fluid,  $\tau_f$ . The particle relaxation time is given by<sup>29</sup>

$$\tau_p = \frac{\rho_p d_p^2}{18\mu} \quad (1)$$

where  $\rho_p$  is the particle density,  $d_p$  its diameter, and  $\mu$  the fluid viscosity. For the olive oil particles used  $\tau_p$  was calculated as  $2.2 \mu s$ . The characteristic time of the fluid is represented by  $\tau_f = L/U_p$ ,<sup>30,31</sup> where  $L$  is a characteristic length, and  $U_p$  is the maximum induced velocity behind the shock wave. The case of the maximum flow velocity is used since at these flow conditions the ability of the tracer particles to follow the fluid motion is most crucial. For  $L$  we have used the equivalent circle diameter of each nozzle. Therefore, the Stokes numbers are calculated as  $3.12 \times 10^{-3}$  and  $1.97 \times 10^{-3}$  for the nozzles with axis ratios  $a/b = 0.2$  and  $0.5$ , respectively. Therefore the  $1 \mu m$  seed particles followed closely the fluid motion changes.

A synchroniser allows control of the laser firing and image acquisition by the camera, and has the facility for external inputs for triggering the PIV system. A high specification PC with *TSI's Insight PIV* software installed enables data download and analysis. In addition, *TecPlot 10* is also loaded for data display and analysis (with *TSI Plot PIV* add-on). The size of the interrogation zones ( $32 \times 32$  pixels) and the timing between the two PIV frames ( $\Delta t = 3 \mu s$ ) was chosen based on the theoretical Mach number of the flow behind the incident shock wave and the schlieren and shadowgraphs of the flow which were obtained prior to the PIV experiments. For each diaphragm pressure ratio  $P_4/P_1$  the theoretical induced velocity behind the incident shock can be determined by the well known shock tube relations given by Anderson 1990.<sup>32</sup> These correspond to  $U_p = 168, 252$ , and  $301$  m/s for  $P_4/P_1 = 4, 8$ , and  $12$ , respectively. The total interrogation area was approximately  $80 \times 90$  mm.

An enclosure was designed which encased the exit of the shock tube. Prior to each run, this enclosure was filled with tracer particles along with the driven section of the shock tube so that each time the shock tube was fired the flow would discharge into the chamber which was filled with tracer particles.

Two sets of PIV measurements were conducted: in the first case the laser sheet was

placed parallel to the shock tube along the x-axis, and in the second case the laser sheet was placed normal to the direction of the flow at  $X = 10, 25, 50, 80$ , and  $110$  mm from the nozzle exit to capture the head-on flow-field properties perpendicular to the x-axis; with the y-axis in the transverse position in both cases.

#### D. Measurement Uncertainties and Repeatability

Uncertainty estimation given by Holman 1994<sup>33</sup> was used to determine the uncertainties, in the form of error bars, in plotting the various vortex loop properties, such as non-dimensional vortex loop diameter and distance travelled. The non-dimensional vortex loop propagation  $L/a$ , where  $L$  is the distance travelled and  $a$  is the minor axis of the nozzle, is a given function of the independent variables  $L$  and  $a$ . Let  $w_R$  be the uncertainty in the result and  $w_1$  and  $w_2$  be the uncertainties in the independent variables  $L$  and  $a$ . Then the uncertainty in the result is given as

$$w_R = \left[ \left( \frac{\partial(L/a)}{\partial L} w_1 \right)^2 + \left( \frac{\partial(L/a)}{\partial a} w_2 \right)^2 \right]^{1/2}. \quad (2)$$

The uncertainty in measuring the independent variables relates back to the image resolution captured by the CCD camera and the accuracy in pinpointing the flow features under consideration when the images digitised. MATLAB is used to digitise the images and the flow features are located to within  $\pm 1$  pixel accuracy. The accuracy in measuring the non-dimensional vortex loop diameter is also arrived at using the same methodology.

The repeatability of the experiments is determined by: (i) setting the same driver pressure, (ii) having the same delay time output from the delay generator, and (iii) triggering the laser and camera at two consecutive frames separated by  $\Delta t$ . If the repeatability of the system is high enough, then by repeating the mentioned procedure the vortex loop should be captured at roughly the same location.

The aforementioned procedure was repeated twice and the location of the vortex loop for the two cases was compared frame by frame. The maximum difference between the location of the vortex loop for the sets of repeats was calculated as 1.5%.

### III. RESULTS AND DISCUSSIONS

The experimental shock Mach numbers corresponding to the nozzles' exit are obtained from the PIV measurements and provided in Table I. The flow Reynolds numbers are also tabulated in Table I. The  $Re$  number,  $Re = \rho U_p L / \mu$ , is in terms of the density behind the incident shock ( $\rho$ ), the velocity behind the incident shock ( $U_p$ ) obtained from the PIV results, and the dynamic viscosity ( $\mu$ ) corresponding to the flow behind the incident shock. The length scale ( $L$ ) used in the calculation of  $Re$  is the length of the minor axis  $a = 6$  and  $15$  mm. For relatively weak shock waves, such as those considered in the present study, Mirels 1955<sup>34</sup> showed that the boundary layer generated behind the moving shock wave inside the shock tube is a region of laminar flow.

#### A. Exotic Nozzle with Axis Ratio $a/b = 0.2$

As the incident shock wave diffracts at the exit of the nozzle, expansion waves travelling upstream start to form which will accelerate the flow inside the nozzle,<sup>35</sup> this behaviour adds to unsteady nature of the flow. The schlieren photographs of the vortex loop generated from the nozzle having minor to major axis ratio  $a/b = 0.2$ , are presented in Figure 2. The times are given from the instant the incident shock exits the tube. We can immediately notice the incident shock wave, the compressible vortex loop, and the shock cells formed as a consequence of internal reflections visible in the wake of the vortex loop. The experimental work of Howard and Matthews 1956<sup>36</sup> and the numerical work of Sun and Takayama 2003<sup>37</sup> and Sivier et al. 1992<sup>38</sup> of shock wave diffractions showed that the vorticity produced by the shear layer represents a large proportion of the total vorticity. The shear layer is formed due to the separation of the boundary layer attached to the upstream wall. Behind a curved shock caused by the geometric expansion, the pressure and density gradients are not parallel to each other, which, as given in the baroclinic torque term, also contribute to the creation of vorticity in shock wave diffraction.

Due to the three-dimensional nature of the flow field, the vortex structure adopts a deformed torus shape. The vortex loop in Figure 2(a) has a convex front to the right, indicative that the portions of the vortex loop formed along the singular corners travel faster downstream. However, in Figure 2(b), we see that the vortex loops portions along the



top and bottom have begun to move downstream at a relative velocity greater than the rest of the vortex loop i.e., the portions generated through the singular corners, evident from the curling in the downstream direction of these regions.

The schlieren photographs of the flow at a diaphragm pressure ratio of  $P_4/P_1 = 8$  are given in Figure 3, with views from two perspectives. In Figure 3(a) the ‘entire’ shock front is visible as a distinct sharp line. In Figure 3(b) however, the portions of the incident shock diffracted from the singular corners are almost invisible. This suggests a reduction in the compression across the shock front upon diffraction from the corners. The embedded shock wave present in the centre of the vortex loop in Figure 3(b) is indicative of the vortex flow being supersonic in the sense that the on-axis flow is supersonic in the frame of reference of the vortex loop. The differential interferometry study of Baird 1986<sup>39</sup> showed that the embedded shock appears once the vortex loop is formed and travelled downstream. The presence of the embedded shock wave matches the low pressure gas entering the vortex loop through the nozzle to the upstream ambient air. The difference in vortex loop propagation velocity, previously mentioned for the lower driver pressure, is also present at a higher diaphragm pressure ratio.

The head-on PIV result of Figure 4 shows the velocity magnitude computed as  $\sqrt{U^2 + V^2}$ , for a diaphragm pressure ratio of  $P_4/P_1 = 4$ . The vectors present in the upper portion of the figure are due to reflection of the laser light from the nozzle surface and do not affect the accuracy of the results. The induced velocity is two-fold: (i) that of the incident shock, and (ii) the induced flow-field as a consequent motion of the vortex loop. As described earlier in the schlieren images, the sharp discontinuity which is the shock wave diffracted from the corners was not evident. This fact can be corroborated when observing the velocity field of Figure 4, where compared to the rest of the nozzle, the flow has a very weak velocity profile.

Results of the PIV experiments performed at  $P_4/P_1 = 4$  on the exotic nozzle having  $a/b = 0.2$ , are shown in Figure 5. The colours present the vorticity profile calculated as  $\omega_z = \frac{\partial u}{\partial y} - \frac{\partial v}{\partial x}$ , while the vectors show the velocity magnitude, with the magnitude of the velocity being proportional to the length of the vectors. There exist different types of vortex loops: (i) those where turbulence initiates naturally at the nozzle of the generator, and (ii) vortex loops that are initially laminar and undergo natural transition to turbulence by azimuthal bending instabilities. During the laminar phase, the core structure is highly concentrated with peak vorticity values as shown in the PIV data of Figure 5(a). Azimuthal

bending instabilities mark the beginning of the transition stage. The upper and lower cores become deformed and show signs of the turbulent breakup (Figure 5(b)). The turbulent stage is characterised by a strong shedding process into the wake of the vortex loop, indicated by the formation of small and concentrated vorticity regions in the periphery of the core regions such as those of Figure 5(c). However, the vorticity distribution in the core region remains concentrated. In Figure 5(c), two cores of concentrated vorticity appear ahead of the main vortex cores. The raw PIV images indicate that as the primary vortex cores move away from each other, tending to increase the diameter of the primary vortex, it allows the jet exiting the tube to pass through it, but its circulation influences the jet downstream of the loop. Hence, the new vortex cores have a circulation in the same direction as the primary vortex cores with the upper core rotating counter clock-wise and the lower core having a clock-wise rotation. The instability vortices present in the jet shear layer of Figure 5(c), are generated near the nozzle lip and grow as they propagate downstream manifesting themselves as large-scale vortical structures.<sup>41,42</sup>

The behaviour of the vortex loop generated at a diaphragm pressure ratio of  $P_4/P_1 = 12$  is visualised and quantified in the results of Figure 6. The obvious distinction between the flow of Figure 6 and that of Figure 5, is the relative size of the vortex loop, deduced from the raw PIV images, and the size of the region of influence of the vortex cores, deduced from the vorticity contours. The maximum vorticity occurs in the region just ahead of the two vortex cores where the flow is deflected outwards (Figure 6(a)). At the same time the two vortex cores are inclined  $30^\circ$  to the horizontal. As the vortex loop travels downstream and its diameter increases, small vortices appear at its apex (see Figure 6(b)). These are more evident than the lower driver pressure and increase in number with distance downstream (Figure 6(c)). The generation of these vortices is due to the generation of a shear layer as a result of the presence of the embedded shock. However, due to the lack of spatial resolution of the PIV system, these vortices are not captured in the processed PIV results.

Examining Figures 6(b) and 6(c) carefully, we notice a slight bulging of the shear layer, which occurs a distance equal to the nozzle width downstream (i.e., 6 mm). After this bulged region, the thickness of the flow pattern remains constant until the vortex loop. The velocity vectors in the aforementioned series of results show an acceleration of the flow starting from this bulged region until the apex of the vortex loop.

As the primary vortex loop travels downstream, two events take place which lead to its

annihilation: (i) instability vortices which are fed through the shear layer into the vortex loop, and (ii) vorticity dumped into the surrounding potential flow due to viscous diffusion.<sup>43</sup> The instability vortices travel along the shear layer of the jet exiting the nozzle and go through the vortex loop, coming out the front they move around the periphery of the vortex loop and go through the same cycle. Hence, in a way the vortex loop itself is responsible for its destabilisation. The relative influence of items (i) and (ii) is unknown.

Figures 7(a) and 7(b) depict how the jet growth rate along the minor axis of the nozzle results in the vertical stretching of the jet as the vortex loop approaches the location of the laser sheet. The extremum of velocities is reminiscent of the shape of the vortex loop. Figures 7(d) and 7(f) represent the vorticity maps generated due to the presence of axial vorticity ( $\omega_x = \frac{\partial w}{\partial y} - \frac{\partial v}{\partial z}$ ) corresponding to Figures 7(c) and 7(e), respectively. As the vortex loop arrives at the location of the laser sheet in Figure 7(c), the magnitude of the induced outwards velocity reduces. This is because at this location the circulation of the vortex loop causes an acceleration of the flow backwards (into the page). At this instant, the vorticity map of Figures 7(d) reveals regions of concentrated vorticity present in the four corners of the jet. Because these regions of vorticity are relatively distant from each other, the so called ‘vortex pair’ interaction does not come into play. The vortex pairs play a critical role in the induced velocity. If we examine the velocity and vorticity maps of Figures 7(e) and 7(f), we can see that the vortices have paired-up and in the regions between them they cause an acceleration of the flow. The presence of these vortices is due to the existence of longitudinal vortex structures.

In Figure 8 the diameter and distance travelled by the vortex loop is non-dimensionalised with reference to the minor axis of the nozzle  $a$ , for the three different diaphragm pressure ratios. The dimensionless time  $(t - t_1) \times U_s/a$  is based on the specified time  $t$ , the time when the entire loop has exited the nozzle  $t_1$ , and the corresponding shock wave velocity  $U_s$ . Both the rate of growth of the vortex loop and the distance travelled, are independent of flow Reynolds number.

### **B. Exotic Nozzle with Axis Ratio $a/b = 0.5$**

At a lower flow Reynolds number the vorticity is more concentrated with the vortex cores having a circular cross section. This can be readily seen in Figure 9(a) with a flow Reynolds

number of  $Re = 1.1 \times 10^5$ , compared to Figure 10(a) with  $Re = 3.7 \times 10^5$ , where the vorticity is spread in the stream-wise direction as a result of higher translational velocity. Due to high magnitudes of vorticity, it is difficult to obtain quantitative data of the vortex core, as can be seen from Figure 9(a). The tracer particles, being a few orders of magnitude denser than the gas, are centrifuged out of the vortex core.

As the vorticity diffuses out of the body of moving fluid into the outer irrotational fluid, it has two effects: it causes some of the fluid, with newly acquired vorticity to be entrained, while the rest is left behind and accounts for the appearance of vorticity in the wake (Figures 9(b) and 10(b)).<sup>40,43</sup> Kelvin-Helmholtz (K-H) shear layer instabilities on the gas front of the jet, also generates vortices behind the primary vortex loop.<sup>44</sup>

Figure 11 represents the side view of the flow-field at a pressure ratio of  $P_4/P_1 = 12$ . The deceleration of the flow ahead of the embedded shock leads to the generation of a shear layer. As a result of Kelvin-Helmholtz instabilities a counter-rotating vortex forms at the apex of the primary vortex loop. The motion of the counter-rotating vortex can be traced in the series of images of Figure 11. Since it is a counter-rotating vortex, its tendency is to travel upstream around the periphery of the primary vortex and into its wake.

The type of complex shock structure formed by a shock-vortex interaction is dependent on the Mach number of the incident shock wave. This dictates the severity of the interaction between the embedded shock and the vortex loop. Weak interactions involve slight deformation of the shock and the acoustic wave generation whilst strong interactions involve significant deformation of the shock wave due to the vortex and may include the production of secondary shocks due to the shock splitting phenomenon.<sup>45</sup>

The embedded shock, which is visible in the sequence of photographs of Figure 12 is carried along at the same speed as the vortex loop.<sup>46</sup> These are taken at the same times as the images of Figure 11. The shock wave is a rearward facing shock such that there is low pressure to the left of the shock and high pressure to the right. The counter-rotating vortex mentioned in Figure 11 is also visible in Figures 12(a) and 12(c). The oblique shock waves behind the vortex loop lead to the generation of a convergent-divergent flow pattern highlighted in Figure 12(a). This is due to the Mach reflection of the shock waves within the jet.

Although the embedded shock starts off planar, it oscillates in space as seen in Figures 12(b) to 12(c), and the deceleration of the flow generates a small cavity at the apex of the

vortex loop, not visible in the series of images of Figure 11.

The laser sheet which slices the flow-field, illuminates quite clearly the formation of the counter-rotating vortex and the deceleration of the flow caused by the embedded shock in Figure 13(a). The newly formed vortex, rolls over the periphery of the primary loop and moves in the upstream direction with respect to the primary loop in Figure 13(b). Eventually it is ejected from the primary loop, continues to move in the upstream direction relative to the primary loop and interacts with the trailing jet. The magnitude of the vorticity of the primary loop changes as it interacts with the secondary one tending to decrease. This is because once the counter-rotating vortex loop is aligned vertically with the primary loop, the circulation of the secondary vortex loop reduces the vorticity magnitude of the primary one, since they are acting in opposite directions.

Because of the high  $Re$  number the flow is quite turbulent for the larger nozzle and this is identified in the velocity profile of Figure 14(a). The vortex instability is also accompanied by the formation of secondary vortical structures on the inner core of the vortex loop. These are visible in the vorticity plot of Figure 14(d). The secondary vortical structures were also identified in the experimental work performed by Dazin et al. 2006<sup>47</sup> but for incompressible vortex loops created in water having a significantly lower  $Re$  number. As the vortex loop begins to decay, an increased amount of vorticity is dumped into the wake in the form of secondary vortex structures. Figures 14(b) and 14(e) show the flow properties in the wake of the vortex loop. The secondary vortex structures are responsible for the increased amount of vortex structure of Figure 14(e). The direct numerical simulations of a turbulent vortex loop with  $Re_\Gamma = 7500$  performed by Bergdorf et al. 2007<sup>48</sup>, even though at a relatively lower  $Re$  number, also showed the presence of these structures within the vortex loop wake. Their findings also showed that as the vortex structures propagate downstream, hairpin vortices which are the remainder of the secondary structures are present in the wake. The hairpin vortices account for the small concentrated vortices far in the vortex loop wake of Figures 14(c) and 14(f). The presence of the secondary and hairpin vortices was also corroborated in the simulations of Archer et al. 2008.<sup>49</sup>

As the vortex loop forms at the exit of the nozzle in Figure 15(a), a pair of counter rotating vortices visible in Figure 15(d) is created at the locations of the singular corners (the velocity and vorticity scales, colour bars, of the subplots of Figure 15 are adjusted to allow for better identification of the flow features). The vortex pairs are created due to the

difference in spreading rate of the emerging jet. As the flow evolves downstream in Figure 15(b), it is clearly evident that the jet along the minor axis has a greater spreading rate deduced from the higher magnitudes of velocity. This characteristic results in axis-switching of the jet. This implies that flow exiting from the corner regions has a greater downstream velocity. At the same instant, the regions of concentrated vorticity which were initially paired-up, separate and occupy the four corners. Examining the velocity and vorticity field in the wake of the vortex loop in Figures 15(c) and 15(f), the velocity profile is similar to the induced velocity ahead of the vortex loop, with the maxima occurring in the upper and lower regions. This behaviour indicates that the vortex loop, which is located downstream of the laser sheet, is being compressed vertically so that the vortex filament takes the shape which it originally had when leaving the vicinity of the nozzle. The vortex pairs again pair-up in Figure 15(f) similar to their initial arrangement.

With increasing driver pressure, and hence Mach number, the shear layer increases its angle relative to the horizontal.<sup>44</sup> This causes the diameter of the vortex loop to be innately larger at higher Mach numbers, as shown in Figure 16(a). Compared to the smaller nozzle (see Figure 8(a)), the variation in vortex loop diameter at different Reynolds numbers is more pronounced for the larger nozzle. Although the diameter of the vortex loop tends to initially increase, after approximately 10 time steps, the diameter does not change with distance travelled downstream. For  $P_4/P_1 = 12$ , the diameter even begins to reduce. The gradual increase and afterwards reduction in vortex loop diameter is believed to be due to the presence of the counter-rotating vortex loop. Once the counter-rotating vortex has past the periphery of the main loop, the opposite circulation tends to stretch the diameter of the primary vortex loop as shown in Figure 17. As the counter-rotating vortex moves into the wake of the primary one, its effect is no longer felt and the diameter of the primary vortex loop reduces.

The distance propagated by the vortex loop shown in Figure 16(b) for  $P_4/P_1 = 4, 8$  and 12 follows a linear trend, being faster for the higher driver pressure case. The vortex loop generated by the lowest pressure ratio initially accelerates up to a distance three times the width of the nozzle, indicated by the increased gradient of the points, but decelerates soon after. The action of viscous diffusion thickens the vortex loop and slows it as its diameter increases due to the conservation of momentum.

### C. Conclusions

The present study examined the shock wave and consequent vortex loop generated when a shock tube with various nozzle geometries is employed. Two eye-shaped nozzles with the corner joints representing singularities were studied. The length of the minor axes are  $a = 6$  and  $15$  mm, having a common major axis length of  $30$  mm. The experiments were performed for driver gas (air) pressures of  $P_4 = 4, 8$ , and  $12$  bar; with the pressure in the driven section ( $P_1$ ) being atmospheric. Using qualitative schlieren and shadowgraphy along with the quantitative analysis of the PIV technique, the behaviour of the diffracted shock and vortex loops generated were examined.

The sharp discontinuity which represents the diffracted shock front, did not appear in the schlieren or shadowgraph images of the flow from the singular corners. Head-on PIV measurements with the laser sheet normal to the nozzle axis, corroborated this finding by showing a significant reduction in flow velocity exiting from the singular segments of the nozzle.

A vortex loop is created by the impulsive ejection of fluid through the shock tube. Viscous diffusion of the momentum contained in the vortex loop core causes the diameter to grow, with ambient fluid being engulfed, or entrained, into the core. The total circulation then decays, thereby decreasing the velocity of propagation of the vortex loop. This decaying process leads to eventual annihilation of all vorticity contained in a vortex.

At diaphragm pressure ratios of  $P_4/P_1 = 8$  and  $12$ , a rearward facing embedded shock appears in the core of the vortex loops. The adverse pressure gradient due to the embedded shock causes the flow to decelerate near the central region, which results in a strong velocity gradient. Thus, a shear layer is formed ahead of the primary vortex loop which rolls up due to Kelvin-Helmholtz instability into a counter rotating vortex loop. The resultant interaction between the primary and counter rotating vortex loops causes the counter rotating loop to move around the periphery of the primary one and hence reduces its diameter.

Comparison of the diameter of the vortex loops, when the nozzles' major axis is horizontal, shows that the smaller nozzle with axis ratio  $0.2$  creates vortex loops of greater diameter. This is because the process of axis switching occurs earlier for the smaller nozzle because of the shorter distance necessary for the jet width along the initial minor axis to overtake the width in the other axis. At higher values of diaphragm pressure ratio,  $P_4/P_1$ , and hence

flow Mach number, the effects of compressibility on the propagation of the vortex loops becomes pronounced. Although the measured induced velocity behind the diffracted shock wave varies over 100 m/s for the extremum of diaphragm pressure ratios, the propagation of the vortex loops appear independent of flow Mach number; suggesting that the vortex loops created at higher flow Mach numbers are decelerated.

Comparison between the streamwise ( $\omega_z$ ) and spanwise ( $\omega_x$ ) vorticity contours showed a larger magnitude of vorticity for the streamwise case, almost double in some for the nozzle with axis ratio 0.5 and  $P_4/P_1 = 12$ . The spanwise vorticity plots also revealed the existence of longitudinal vortical structures surrounding the primary vortex loop structure.

A feature that is present in all the cases studied is the presence of the instability vortices in the wake of the main vortex loop which have their origins as instability waves near the nozzle lip. Although these tiny instabilities start off as very weak in strength and are present only along the shear layer, they become stronger. It is these random disturbances which are fed through the shear layer into the vortex loop and eventually give rise to azimuthal disturbances leading to the random motion of the flow.

Due to high magnitudes of vorticity, it is difficult to obtain quantitative data of the vortex core. Perhaps conducting PIV experiments underwater would provide more insight into the relationship between exit velocity and vortex core properties. This relationship could then be applied to compressible flows. Further PIV measurements will be undertaken, to analyse the vortex loops generated by rotating the nozzles so that we are looking at the vortex loops from a different perspective.

## Acknowledgments

The authors are indebted to the technical staff at The University of Manchester for their assistance and for the help and advice of Dr. Martin Hyde (*TSI*) for the installation and setup of the PIV system. The support of the EPSRC Engineering Instrument Pool especially Mr. Adrian Walker, for the loan of the PIV system is greatly acknowledged.



- 
- <sup>1</sup> Prangé, R., Pallier, L., Hansen, K.C., Howard, R., Vourlidis, A., Courtin, R., Parkinson, C., “An interplanetary shock traced by planetary auroral storms from the Sun to Saturn,” *Nature* **432**, pp. 78–81, (2004).
- <sup>2</sup> Shepherd, J.E., Schultz, E., Akbar, R., “Detonation diffraction,” In: Ball, G., Hillier, R., Roberts, G., (eds.) *Proceedings of the 22nd International Symposium on Shock Waves* **1**, pp. 41–48, (2000).
- <sup>3</sup> Ohyagi, S., Obara, T., Hoshi, S., Cai, P., Yoshihashi, T., “Diffraction and re-initiation of detonations behind a backward-facing step,” *Shock Waves* **12**, pp. 221–226, (2002).
- <sup>4</sup> Wilson, J., Sgondea, A., Paxson, D.E., Rosenthal, B.N., “Parametric investigation of thrust augmentation by ejectors on a pulsed detonation tube,” *Journal of Propulsion and Power*, **23**, pp. 108–115, (2007).
- <sup>5</sup> Dziedzic, M., Leutheusser, H.J., “An experimental study of viscous vortex rings,” *Experiments in Fluids* **21**, pp. 315–324, (1996).
- <sup>6</sup> Takamoto, M., Izumi, K., “Experimental observation of stable arrangement of vortex rings,” *Physics of Fluids* **24**, pp. 1582–1583, (1981).
- <sup>7</sup> Dhanak, M.R., DeBernardinis, B., “The evolution of an elliptic vortex ring,” *Journal of Fluid Mechanics* **109**, pp. 189–216, (1981).
- <sup>8</sup> Oshima, Y., Izutsu, N., Oshima, K., Hussain, A.K.M.F., “Bifurcation of an elliptic vortex ring,” *Fluid Dynamics Research* **3**, pp. 133–139, (1988).
- <sup>9</sup> Grinstein, F.F., DeVore, C.R., “Dynamics of coherent structures and transition to turbulence in free square jets,” *Physics of Fluids* **8**, pp. 1237–1251, (1996).
- <sup>10</sup> Yoon, J.H., Lee, S.J., “Investigation of the near-field structure of an elliptic jet using stereoscopic particle image velocimetry,” *Measurement Science and Technology* **14**, pp. 2034–2046, (2003).
- <sup>11</sup> Shusser, M., Gharib, M., “Energy and velocity of a forming vortex ring,” *Physics of Fluids* **12**, pp. 618–621, (2000).
- <sup>12</sup> Zhao, W., Frankel, S.H., Mongeau, L.G., “Effects of trailing jet instability on vortex ring formation,” *Physics of Fluids* **12**, pp. 589–596, (2000).
- <sup>13</sup> Jiang, Z., Onodera, O., Takayama, K., “Evolution of shock waves and the primary vortex loop discharged from a square cross-section tube,” *Shock Waves* **9**, pp. 1–10, (1999).

- <sup>14</sup> Minota, T., “Interaction of a shock wave with a high-speed vortex ring,” *Fluid Dynamics Research* **12**, pp. 335–342, (1993).
- <sup>15</sup> Bykovets, A. P., Repin, V.B., “Formation of a vortex rings at the open end of a pulsed chamber,” *Combustion, Explosion, and Shock Waves* **16**, pp. 73–77, (1980).
- <sup>16</sup> Moore, D.W., “The effect of compressibility on the speed of propagation of a vortex ring,” *Proceedings of the Royal Society of London. Series A* **397**, pp. 87–97, (1985).
- <sup>17</sup> Takayama, F., Ishii, Y., Sakurai, A., Kambe, T., “Self-intensification in shock wave and vortex interaction,” *Fluid Dynamics Research* **12**, pp. 343–348, (1993).
- <sup>18</sup> Minota, T., Nishida, M., Lee, M.G., “Shock formation by compressible vortex ring impinging on a wall,” *Fluid Dynamics Research* **12**, pp. 139–157, (1997).
- <sup>19</sup> Tokugawa, N., Ishii, Y., Sugano, K., Takayama, F., Kambe, T., “Observation and analysis of scattering interaction between a shock wave and a vortex ring,” *Fluid Dynamics Research* **21**, pp. 185–199, (1997).
- <sup>20</sup> Shimizu, T., Watanabe, Y., Kambe, T., “Scattered waves generated by shock wave and vortex ring interaction,” *Fluid Dynamics Research* **27**, pp. 65–90, (2000).
- <sup>21</sup> Ding, Z., Hussaini, M.Y., Erlebacher, G., Krothapalli, A., “Computational study of shock interaction with a vortex ring,” *Physics of Fluids* **13**, pp. 3033–3048, (2001).
- <sup>22</sup> Nakashima, Y., Inoue, O., “Sound generation by a vortex ring collision with a wall,” *Physics of Fluids* **20**, pp. 126104, (2008).
- <sup>23</sup> Brouillette, M., Hebert, C., “Propagation and interaction of shock-generated vortices,” *Fluid Dynamics Research* **21**, pp. 159–169, (1997).
- <sup>24</sup> Kontis, K., An, R., Zare-Behtash, H., Kounadis, D., “Head-on collision of shock wave induced vortices with solid and perforated walls,” *Physics of Fluids* **20**, (2008).
- <sup>25</sup> Arakeri, J.H., Das, D., Krothapalli, A., Lourenco, L., “Vortex ring formation at the open end of a shock tube: A particle image velocimetry study,” *Physics of Fluids* **16**, pp. 1008–1019, (2004).
- <sup>26</sup> Settles, G.S., “Schlieren and Shadowgraph techniques,” *Springer Verlag*, (2001).
- <sup>27</sup> Kontis, K., Kounadis, D., An, R., Zare-Behtash, H., “Vortex ring interaction studies with a cylinder and a sphere,” *International Journal of Heat and Fluid Flow*, **29**, pp. 1380–1392, (2008).
- <sup>28</sup> Raffel, M., Willert, C.E., Kompenhans, J., “Particle Image Velocimetry,” *Springer*, (1998).

- <sup>29</sup> Melling, A., "Tracer particles and seeding for particle image velocimetry," *Measurement Science and Technology* **8**, pp. 1406–1416, (1997).
- <sup>30</sup> Ortiz-Villafuerte, J., Schmidl, W.D., Hassan, Y.A., "Three-dimensional ptv study of the surrounding flow and wake of a bubble rising in a stagnant liquid," *Experiments in Fluids* **29**, pp. S202–S210, (2000).
- <sup>31</sup> Liu, Z., Zheng, Y., Jia, L., Zhang, Q., "Study of bubble induced flow structure using PIV," *Chemical Engineering Science* **60**, pp. 3537–3552, (2005).
- <sup>32</sup> Anderson, J.D., "Modern Compressible Flow, with Historical Perspective," *McGraw-Hill, Inc*, ed. 2, (1990).
- <sup>33</sup> Holman, J.P., "Experimental Methods for Engineers," *McGraw-Hill, Inc*, (1994).
- <sup>34</sup> Mirels, H., "Laminar boundary layer behind shock advancing into stationary fluid," *NACA TN 3401*, (1955).
- <sup>35</sup> Hillier, R., "Computation of shock wave diffraction at a ninety degrees convex edge," *Shock Waves* **1**, pp. 89–98, (1994).
- <sup>36</sup> Howard, L.N., Matthews, D.L., "On the vortices produced in shock diffraction," *Journal of Applied Physics* **27**, pp. 223–231, (1956).
- <sup>37</sup> Sun, M., Takayama, K., "Vorticity production in shock diffraction," *Journal of Fluid Mechanics* **478**, pp. 237–256, (2003).
- <sup>38</sup> Sivier, S., Loth, E., Baum, J., Löhner, R., "Vorticity produced by shock wave diffraction," *Shock Waves* **2**, pp. 31–41, (1992).
- <sup>39</sup> Baird, J.P., "Supersonic vortex rings," *Proceedings of the Royal Society of London. Series A* **409**, pp. 59–65, (1987).
- <sup>40</sup> Weigand, A., Gharib, M., "On the decay of a turbulent vortex ring," *Physics of Fluids* **6**, pp. 3806–3808, (1994).
- <sup>41</sup> Tam, C., Ahuja, K.K., "Theoretical model of discrete tone generation by impinging jets," *Journal of Fluid Mechanics* **214**, pp. 67–87, (1990).
- <sup>42</sup> Krothapalli, A., Rajkuperan, E., Alvi, F., Lourenco, L., "Flow field and noise characteristics of a supersonic impinging jet," *Journal of Fluid Mechanics* **392**, pp. 155–181, (1999).
- <sup>43</sup> Maxworthy, T., "The structure and stability of vortex rings," *Journal of Fluid Mechanics* **51**, pp. 15–32, (1972).
- <sup>44</sup> Golub, V.V., "Development of shock wave and vortex ring structures in unsteady jets," *Shock*

- Waves* **3**, pp. 279–285, (1994).
- <sup>45</sup> Chatterjee, A., “Shock wave deformation in shock-vortex interactions,” *Shock Waves* **9**, pp. 95–105, (1999).
- <sup>46</sup> Broadbent, E.G., Moore, D.W., “The interaction of a vortex ring and a coaxial supersonic jet,” *Proceedings of the Royal Society of London. Series A* **409**, pp. 47–57, (1987).
- <sup>47</sup> Dazin, A., Dupont, P., Stanislas, M., “Experimental characterization of the instability of the vortex rings. Part II: Non-linear phase,” *Experiments in Fluids* **41**, pp. 401–413, (2006).
- <sup>48</sup> Bergdorf, M., Koumoutsakos, P., Leonard, A., “Direct numerical simulations of vortex rings at  $Re_\Gamma = 7500$ ,” *Journal of Fluid Mechanics* **581**, pp. 495–505, (2007).
- <sup>49</sup> Archer, P.J., Thomas, T.G., Coleman, G.N., “Direct numerical simulation of vortex ring evolution from the laminar to the early turbulent regime,” *Journal of Fluid Mechanics* **598**, pp. 201–226, (2008).

TABLE I: Experimental conditions corresponding to the different nozzles.

Axis ratio	$P_4$ [bar]	$M_{se}$	$Re$ ( $\times 10^5$ )
$a/b = 0.2$	4	1.12	0.8
	8	1.24	3.5
	12	1.35	4.1
$a/b = 0.5$	4	1.16	1.1
	8	1.31	3.7
	12	1.51	4.6

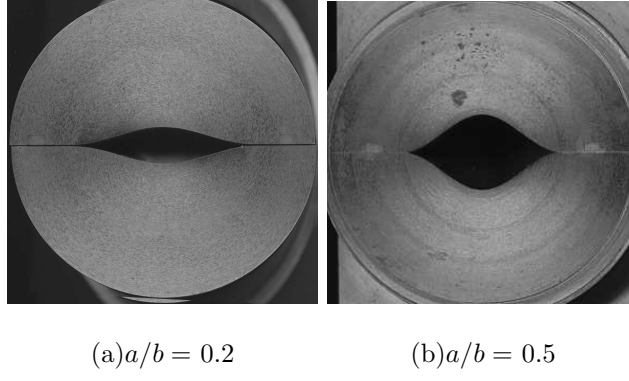


FIG. 1: Eye-shaped nozzles' cross section.

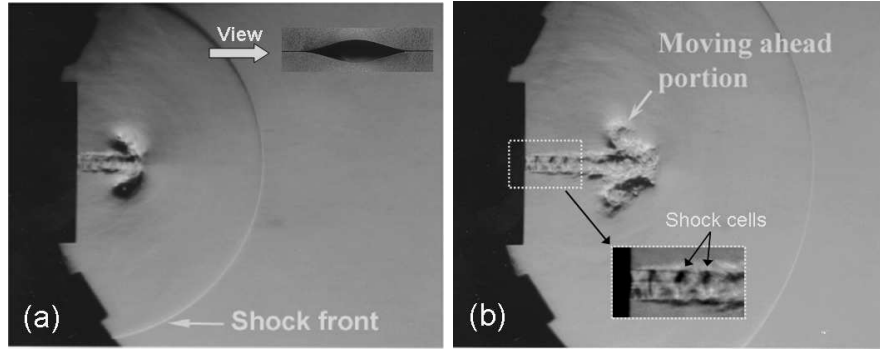


FIG. 2: Schlieren photographs of exotic nozzle  $a/b = 0.2$ , major axis horizontal,  $P_4/P_1 = 4$ ,  $t =$  (a) 0.17 ms (b) 0.25 ms.

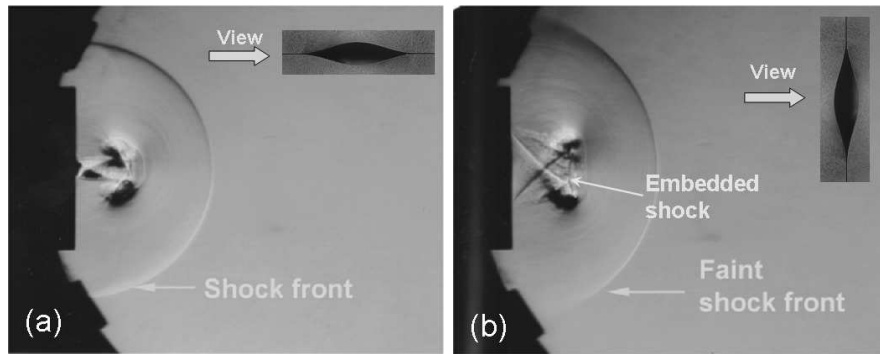


FIG. 3: Schlieren photographs of exotic nozzle  $a/b = 0.2$ ,  $P_4/P_1 = 8$ ,  $t = 0.11$  ms, (a) major axis horizontal, (b) major axis vertical.

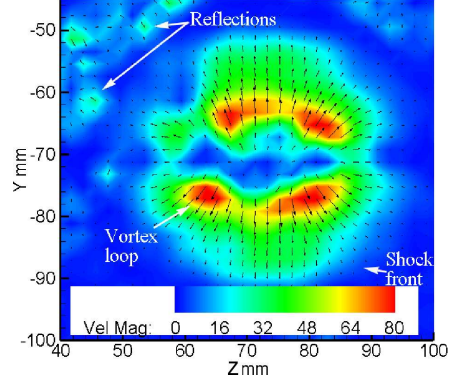


FIG. 4: Head-on PIV result for exotic nozzle  $a/b = 0.2$ , 10 mm from nozzle exit,  $P_4/P_1 = 4$ .

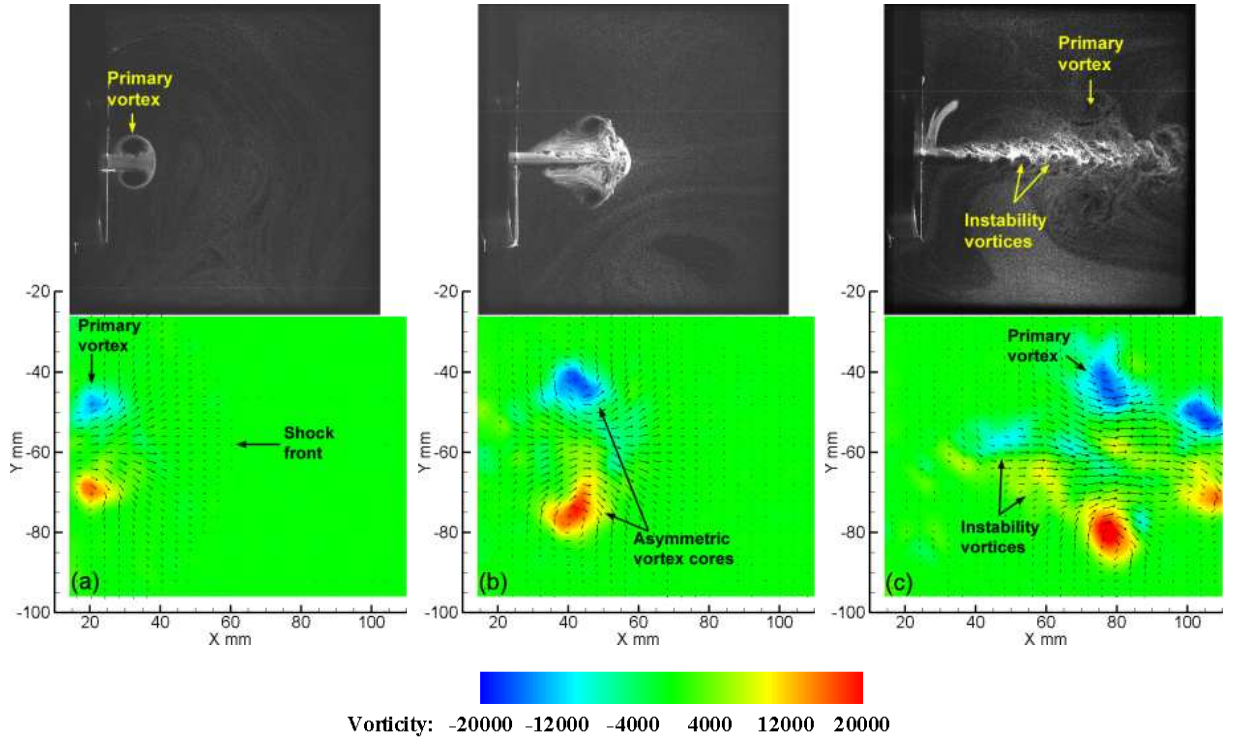


FIG. 5: PIV of exotic nozzle  $a/b = 0.2$ , major axis horizontal,  $P_4/P_1 = 4$ ,  $t =$  (a) 0.11 ms, (b) 0.28 ms, (c) 0.68 ms.

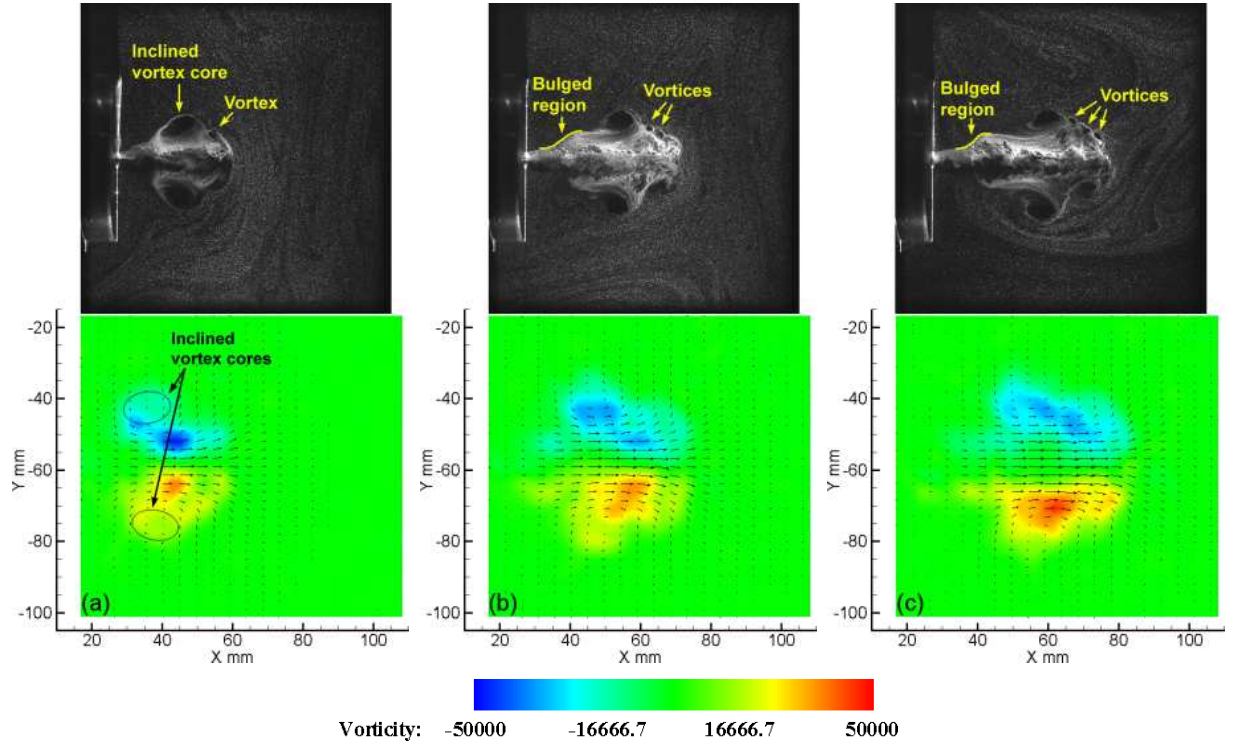


FIG. 6: PIV of exotic nozzle  $a/b = 0.2$ , major axis horizontal,  $P_4/P_1 = 12$ ,  $t = (a) 0.29$  ms,  $(b) 0.34$  ms,  $(c) 0.38$  ms.

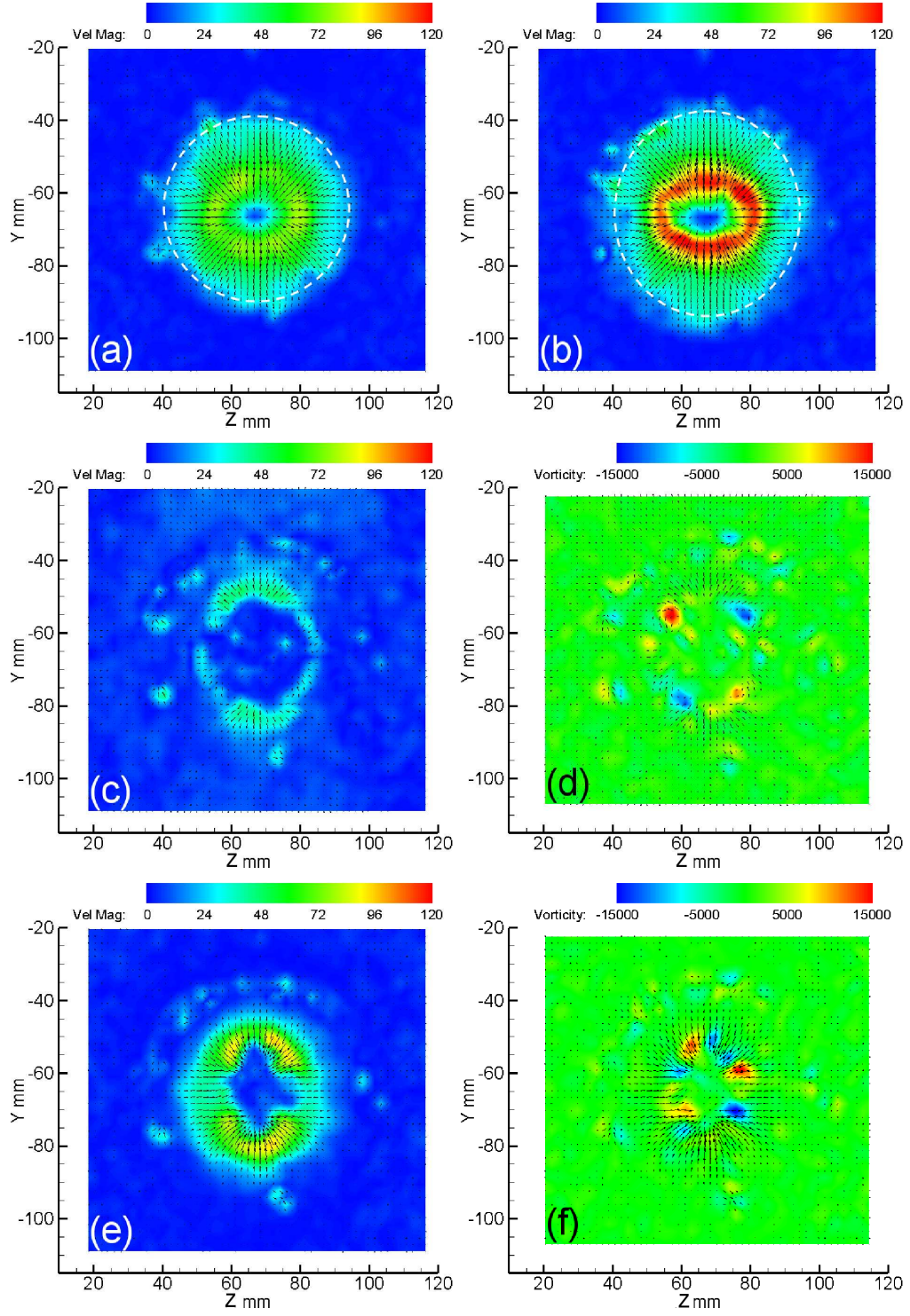


FIG. 7: Head-on PIV of exotic nozzle  $a/b = 0.2$ ,  $P_4/P_1 = 12$ , 25 mm from nozzle exit,  $t =$  (a) 15 ms, (b) 0.18 ms, (c) & (d) 0.22 ms, (e) & (f) 0.27 ms.



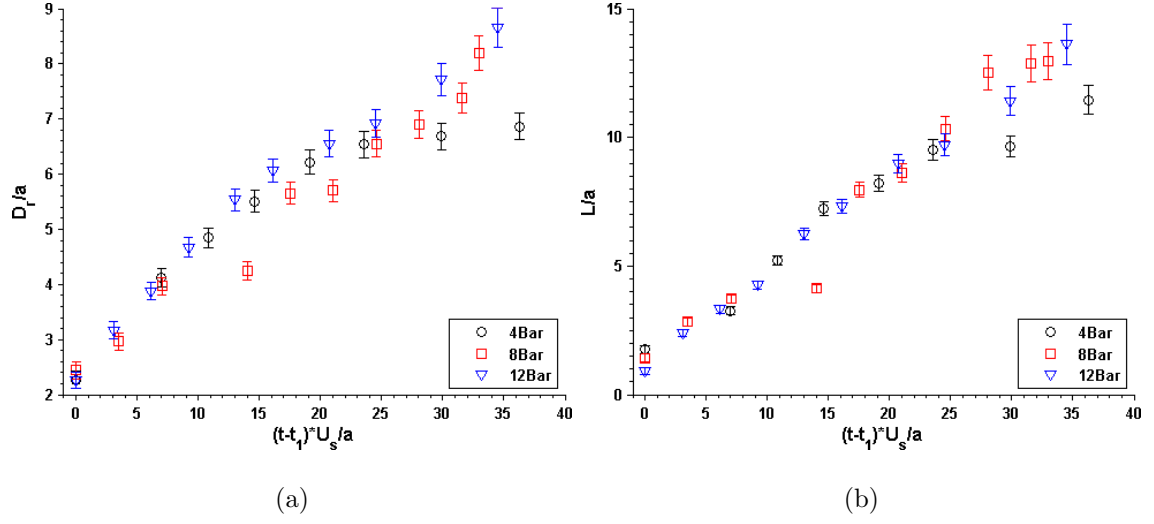


FIG. 8: Exotic nozzle with  $a/b = 0.2$ , variation of: (a) vortex loop diameter, (b) distance propagated by vortex loop.

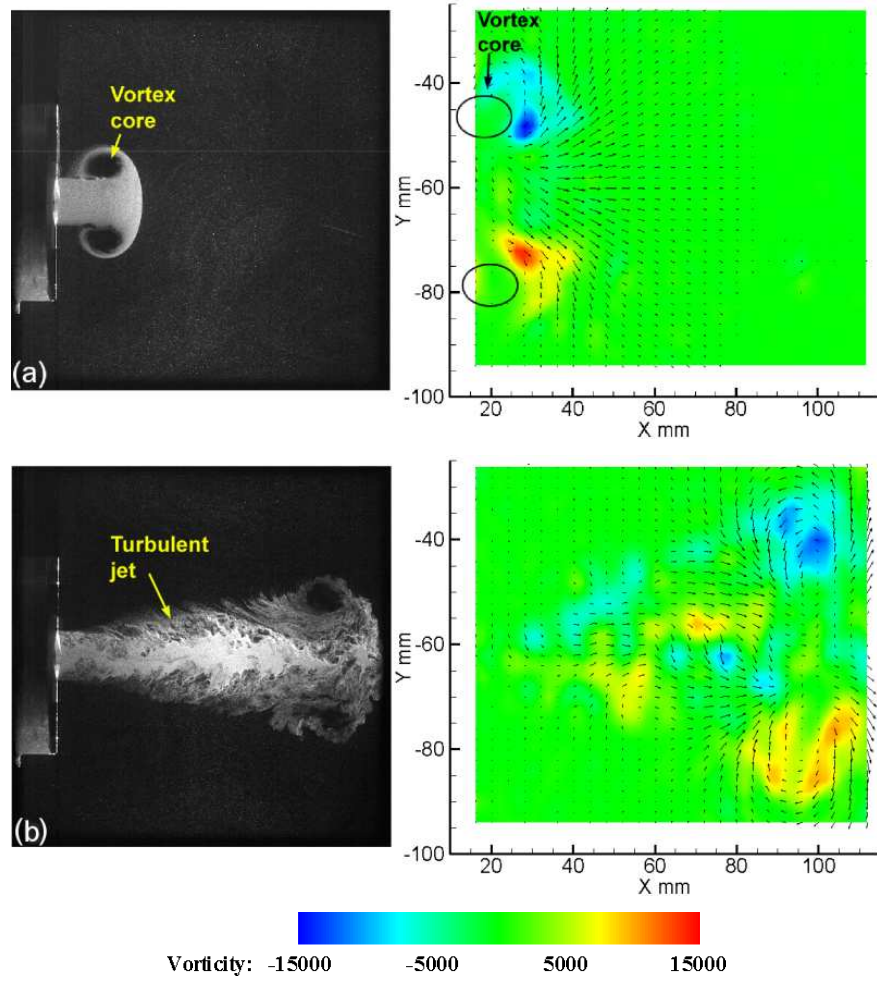


FIG. 9: PIV of exotic nozzle  $a/b = 0.5$ , major axis horizontal,  $P_4/P_1 = 4$ ,  $t =$  (a) 0.23 ms, (b) 1.1 ms.

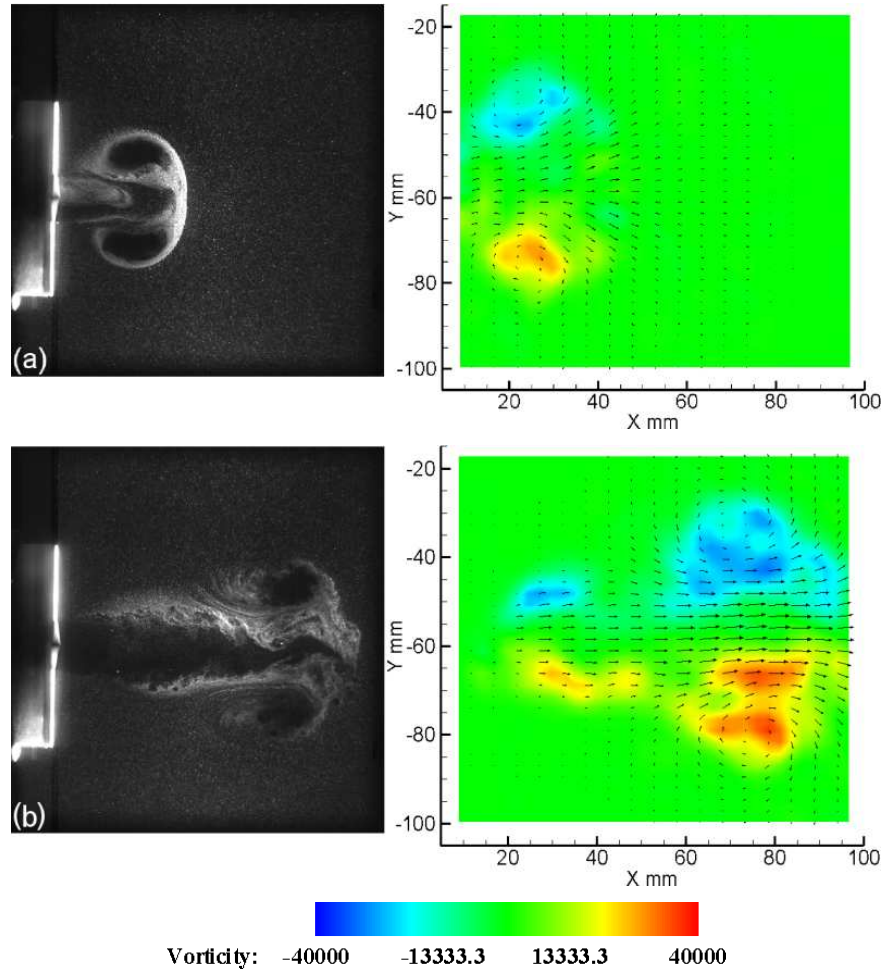


FIG. 10: PIV of exotic nozzle  $a/b = 0.5$ , major axis horizontal,  $P_4/P_1 = 8$ ,  $t =$  (a) 0.16 ms, (b) 0.49 ms.

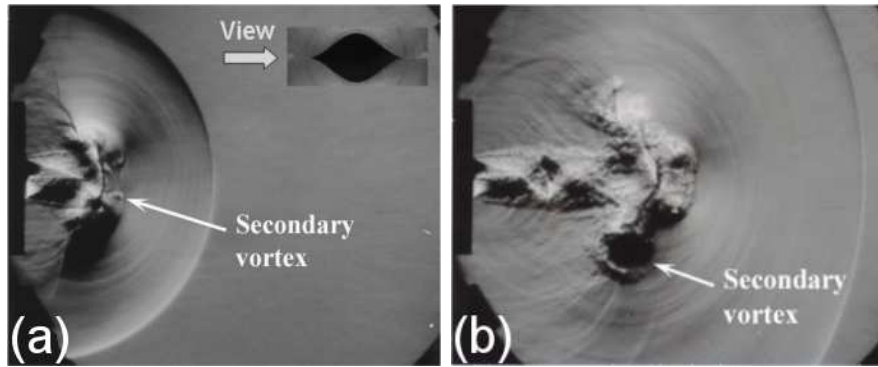


FIG. 11: Schlieren and shadowgraph images of exotic nozzle  $a/b = 0.5$ , major axis horizontal,  $P_4/P_1 = 12$ ,  $t =$  (a) 0.1 ms, (b) 0.32 ms.

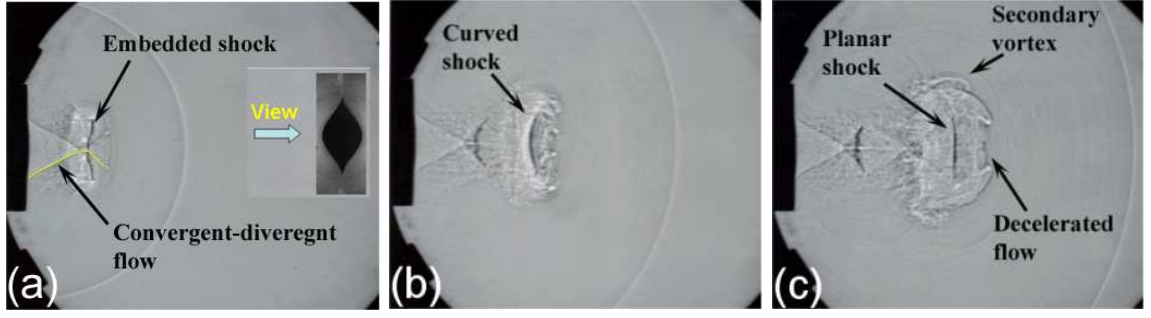


FIG. 12: Schlieren and shadowgraph images of exotic nozzle  $a/b = 0.5$ , major axis vertical,  $P_4/P_1 = 12$ ,  $t =$  (a) 0.1 ms, (b) 0.24 ms, (c) 0.32 ms.

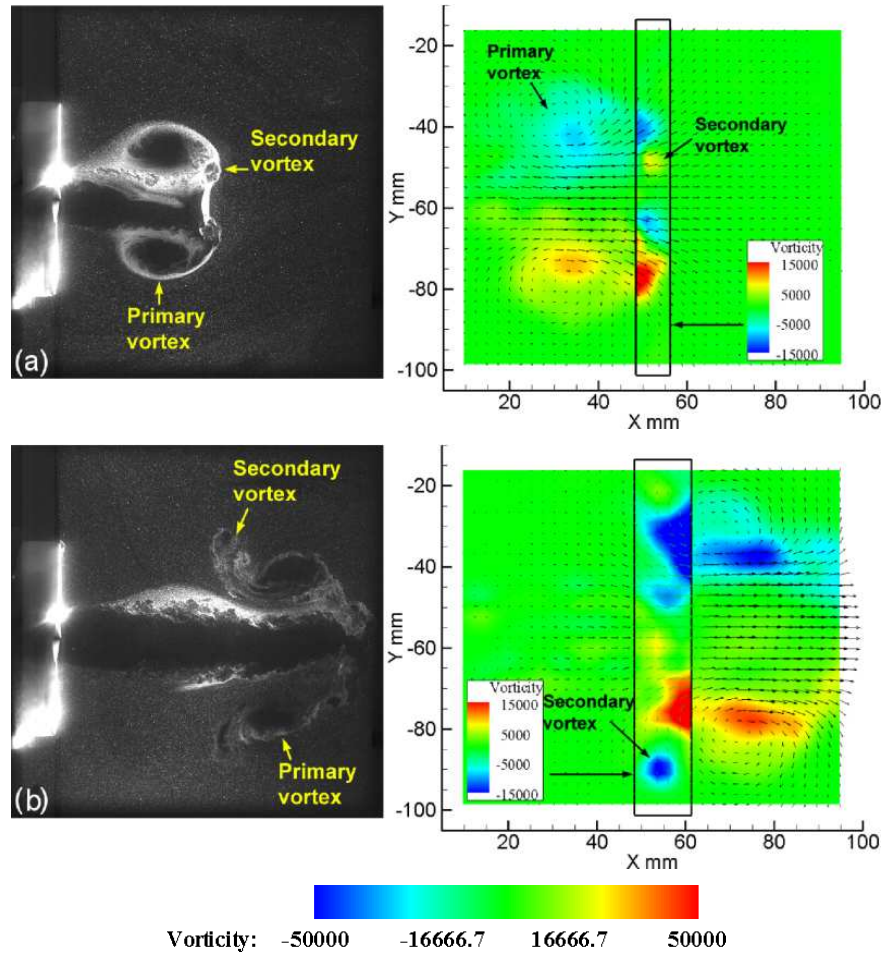


FIG. 13: PIV of exotic nozzle  $a/b = 0.5$ , major axis horizontal,  $P_4/P_1 = 12$ ,  $t =$  (a) 0.19 ms, (b) 0.4 ms.

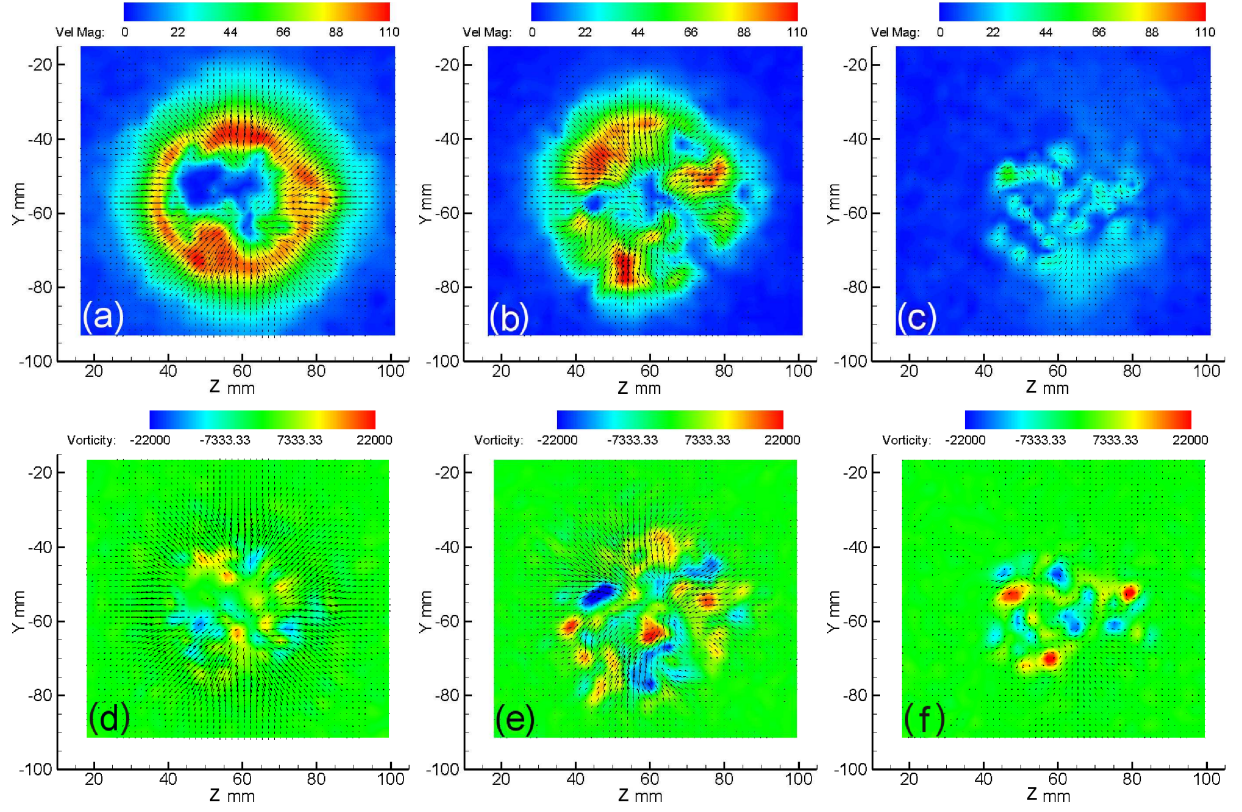


FIG. 14: Head-on PIV of exotic nozzle  $a/b = 0.5$ ,  $P_4/P_1 = 4$ , 80 mm from nozzle exit,  $t =$  (a) & (d) 0.53 ms, (b) & (e) 0.63 ms, (c) & (f) 0.79 ms.



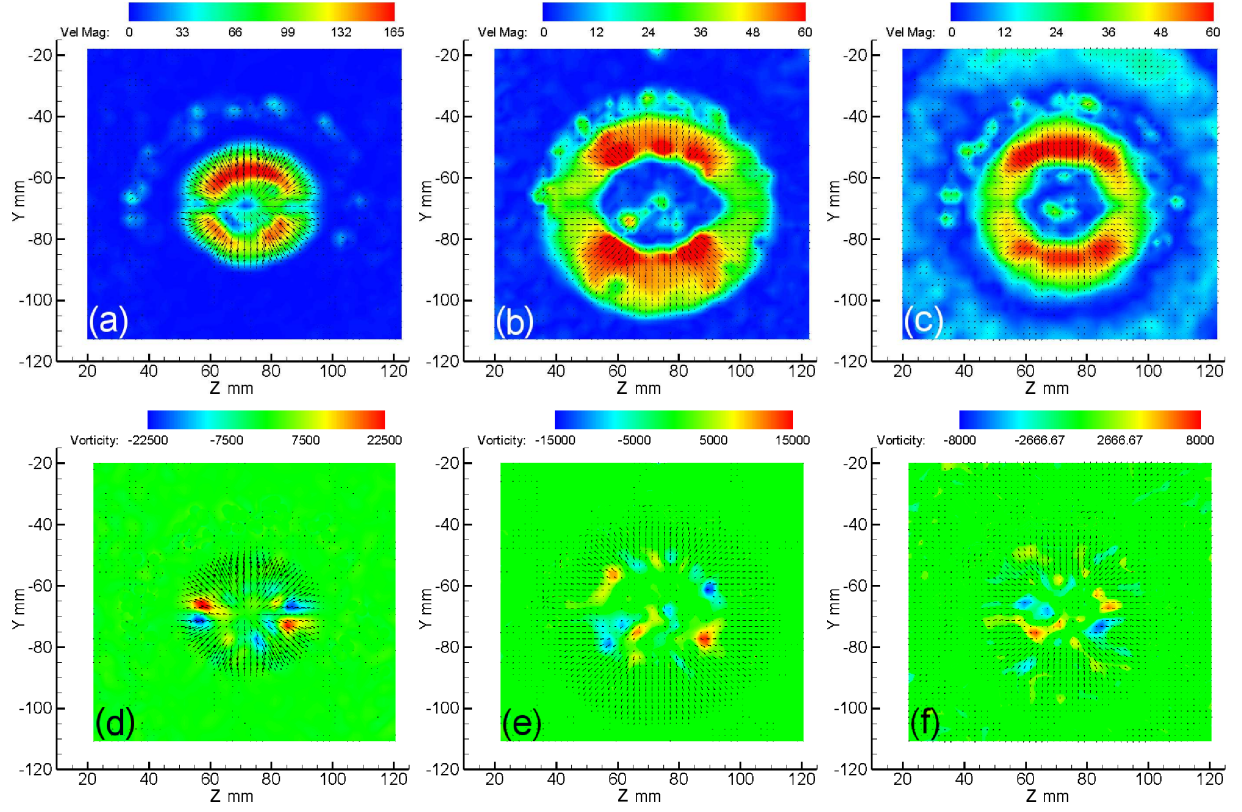


FIG. 15: Head-on PIV of exotic nozzle  $a/b = 0.5$ ,  $P_4/P_1 = 12$ , 10 mm from nozzle exit,  $t =$  (a) & (d) 0.02 ms, (b) & (e) 0.07 ms, (c) & (f) 0.1 ms.

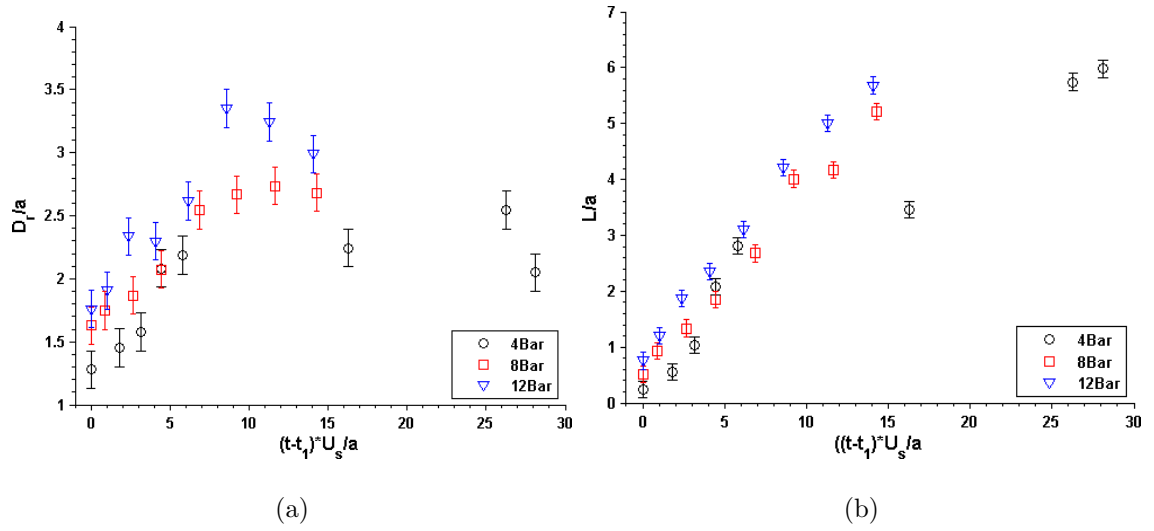


FIG. 16: Exotic nozzle with  $a/b = 0.5$ , variation of: (a) vortex loop diameter, (b) distance propagated by vortex loop.

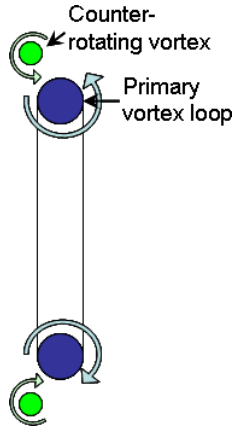


FIG. 17: Stretching of the primary vortex loop by the counter-rotating vortex.